

Unsupervised Deep Learning for Inverse Problems in Computed Tomography

Laura Hellwege^{1,2,*}, Johann Christopher Engster², Moritz
Schaar², Thorsten M. Buzug^{1,2}, Maik Stille²

¹Institute of Medical Engineering, University of Lübeck, 23562 Lübeck,
Germany.

²Fraunhofer Research Institution for Individualized Medical Technology
and Engineering (IMTE), 23562 Lübeck, Germany.

*l.hellwege@uni-luebeck.de.

Abstract

Assume you encounter an inverse problem that shall be solved for a large number of data, but no ground-truth data is available. To emulate this encounter, in this study, we assume it is unknown how to solve the imaging problem of Computed Tomography (CT). An unsupervised deep learning approach is introduced, that leverages the inherent similarities between deep neural network training, deep image prior (DIP) and unrolled optimization schemes. We demonstrate the feasibility of reconstructing images from measurement data by pure network inference, without relying on ground-truth images in the training process or additional gradient steps for unseen samples. Our method is evaluated on the two-dimensional 2DeteCT dataset, showcasing superior performance in terms of mean squared error (MSE) and structural similarity index (SSIM) compared to traditional filtered backprojection (FBP) and maximum likelihood (ML) reconstruction techniques as well as similar performance compared to a supervised DL reconstruction. Additionally, our approach significantly reduces reconstruction time, making it a promising alternative for real-time medical imaging applications. Future work will focus on extending this methodology for adaptability of the projection geometry and other use-cases in medical imaging.

Keywords: Inverse Problems, Physics-Informed Deep Learning, Unsupervised Learning, Imaging, Projection Layers

1 Introduction

Deep learning has emerged as a transformative technology in various fields, including medical imaging. In the context of CT reconstruction, different methods have been developed to enhance image quality through supervised and unsupervised training techniques. Notably, certain approaches that leverage supervised training, i.e. utilizing ground-truth images for calculating training loss, have demonstrated significant improvements in image quality. For instance, *Jin et al.* employed a U-Net architecture in the image domain to enhance reconstruction from sub-sampled projection data[1]. *He and Ma* utilized fully connected layers operating on sinogram data to learn the projection filter step, comparing their reconstructions to ground-truth images for effective supervised training[2]. Similarly, *Li et al.* proposed a FBP-inspired network architecture designed for direct learning from sinogram to image[3] and *Ge et al.* developed a network that integrates both a projection domain unit and an image domain unit, connected by a domain transform layer[4].

As for unsupervised approaches, previously proposed methods rely on deep image priors to replace or enhance steps in conventional iterative reconstruction with DIP [5, 6, 7]. The gap between conventional gradient-based reconstruction and deep learning has been partially closed with the classification of learnable reconstruction problems and unrolled optimization schemes[8], [9] as well as the application of auto-differentiation techniques [10]. However, these approaches are restricted to solving the optimization problem for each dataset individually. They can be classified as learned iterative reconstruction (learned IR) methods. To our knowledge, there exists no approach that leverages the similarities between (1) learned IR for single datasets and (2) network training with large datasets lacking ground-truth information with subsequent amortized inference on unseen data.

Background

We consider the example of CT reconstruction as a typical inverse problem in imaging. The goal is to recover the original image from its projections. Let $f : \mathbb{R}^2 \rightarrow \mathbb{R}$ be the continuous function that represents the imaging object's attenuation values. Assuming a circular measurement trajectory, the geometric forward projection (FP) in computed tomography can be expressed by the Radon transform

$$\text{FP}(f) = \int_{-\infty}^{\infty} \int_0^{2\pi} f(x, y) \cdot \delta(x \cos \gamma + y \sin \gamma - s) d\gamma ds, \quad (1)$$

where δ denotes the Dirac function, γ the projection angle and s the coordinate of the projection path through the object. This continuous form can be transferred to a linear discrete forward problem. Let $\vec{f} \in \mathbb{R}^N$ be the discretized, vectorized form of the image f and let $\vec{p} \in \mathbb{R}^M$ be its FP. Let the discrete version of the Radon transform from Eq. 1 be represented by a system matrix $A \in \mathbb{R}^{M \times N}$, that attributes a contribution of each pixel f_j , $j = 1, \dots, N$, to each projection value p_i , $i = 1, \dots, M$. Then, the system

matrix defines the discrete FP $A\vec{f} = \vec{p}$ as well as the inverse problem

$$\text{Find } \vec{f}, \text{ s.t. } A\vec{f} = \vec{p}. \quad (2)$$

Iterative reconstruction (IR) is a method that aims to progressively improve the reconstructed image \vec{f} while adhering to Eq. 2. Figure 1 visualizes the general procedure. Let $f^k \in \mathbb{R}^N$ be the reconstructed tomogram at the iteration step $k \in \{0, \dots, K\}$. In particular, let f^0 be the initial image, usually selected as a constant image with a very small positive value. To achieve a stepwise approximation of the current image f^k to the underlying true image f^* , a comparison is made between the measurement p itself and the FP of the current image f^k , i.e. $p^k = Af^k$. Assuming a Gaussian distribution of the underlying projection data, the metric of discrepancy or loss \mathcal{L} is chosen as the \mathcal{L}^2 -norm

$$\mathcal{L}(f^k|p) = \|p - p^k\|^2 = \|p - Af^k\|^2. \quad (3)$$

Due to overall differentiability of Eq. 3, the discrepancy \mathcal{L} can be minimized by iterative gradient-based optimization, i.e.

$$f^{k+1} = f^k + \alpha \cdot \mathcal{D}(\nabla f^k), \quad (4)$$

until a predefined stopping criterion is reached. Here, the step width α and the search direction \mathcal{D} are chosen by the respective optimization method, usually in dependence on the gradient ∇f^k . Regarding implementation, it is important to ensure that the matrix A^T satisfies the adjointness condition

$$\langle A\vec{f}, \vec{p} \rangle_{\mathbb{R}^M} = \langle \vec{f}, A^T\vec{p} \rangle_{\mathbb{R}^N} \quad \forall \vec{f} \in \mathbb{R}^N, \forall \vec{p} \in \mathbb{R}^M, \quad (5)$$

where $\langle \cdot, \cdot \rangle$ denotes the scalar product of the Hilbert spaces \mathbb{R}^N and \mathbb{R}^M . This condition needs to be fulfilled for gradient-based optimization since the adjoint matrix A^T is used as the domain transform from projection to image space - known as back projection (BP). When computing the image gradient from the projection differences, adjointness of A^T guarantees appropriate scaling of the gradient values [11].

Scope of this work

Our main contribution is an unsupervised learning approach to image reconstruction, treating it as an inverse problem. We leverage the similarities of traditional network training with amortized inference, DIP and unrolled optimization schemes. Our focus is the feasibility of training a neural network to solve an inverse problem using only the forward model of the imaging system, without relying on any ground-truth images. To demonstrate the efficacy of our method we choose two experiments that learn the accurate filtering of blurred images from simple backprojection for two datasets:

- A** Forward projections (Eq. 1) of provided FBP CT slices acquired from high-precision data. The image evaluation can then be performed with said FBP slices.
- B** Real low-quality projection data. The image quality is compared to the respective high-quality data reconstructions since no real ground-truth is available.

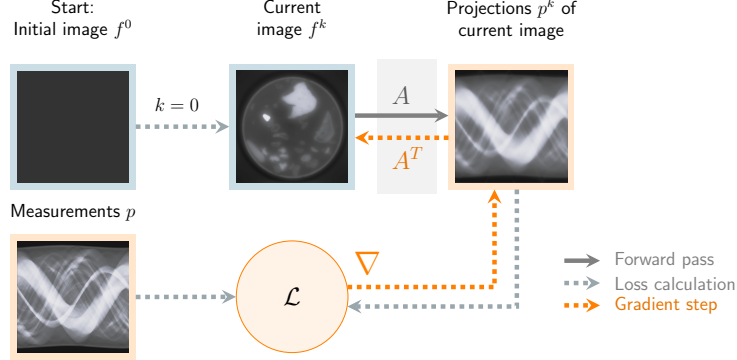


Fig. 1 Gradient-based image reconstruction scheme. The colored boxes indicate the domain of the respective data (orange projection domain, blue image domain). The boxes indicate the domain transform by FP (A) or BP (A^T). The steps to iteratively adapt the current image f^k with the current gradient (∇) are indicated by arrows. The loss \mathcal{L} is defined by Eq. 3.

Methods

Forward and backward projection layers

A critical point of novel deep learning approaches in CT is the incorporation of FP and BP operators into the deep learning framework. These operators enable forward and backward pass computations from the image domain to the projection domain and vice versa. The deep learning framework of this work is implemented in PyTorch[12]. We employ the projector operator definitions of the open-source library *Parallelproj*[13], which was originally designed for positron emission tomography projections utilizing PyTorch compatible tensors. The projection geometry can be defined manually to emulate a circular CT projection trajectory by explicitly defining the respective start and end points of the projection rays. Hence, a projection operator and its adjoint can be incorporated in custom FP and BP network layers. These layers now take advantage of PyTorch’s *autograd* function, such that no manual gradient computations are necessary. The FP and BP of *Parallelproj* are defined mathematically adjoint (Eq. 5), such that iterative computations of gradients are numerically consistent.

Unsupervised training scheme

Figure 2 illustrates our proposed unsupervised training approach. As network input, we only assume knowledge of the projection data p , which is transformed to the image domain by a simple BP (Radon inversion) layer A^T . The resulting blurred image f is fed into a deep convolutional network, namely the U-Net++[14] with the ResNeXt-101 ($32 \times 16d$)[15] encoder. It is important to notice, that training is employed batch-wise on the whole training dataset making it different to previously unrolled optimization schemes. Regarding the implementation, the *Segmentation Models PyTorch*[16] library was employed, offering a pre-built network architecture and encoder as well as loss functions for the PyTorch machine learning framework. The network’s output is the desired high-quality image reconstruction \hat{f} . To enable unsupervised training, the forward pass through the network is completed with

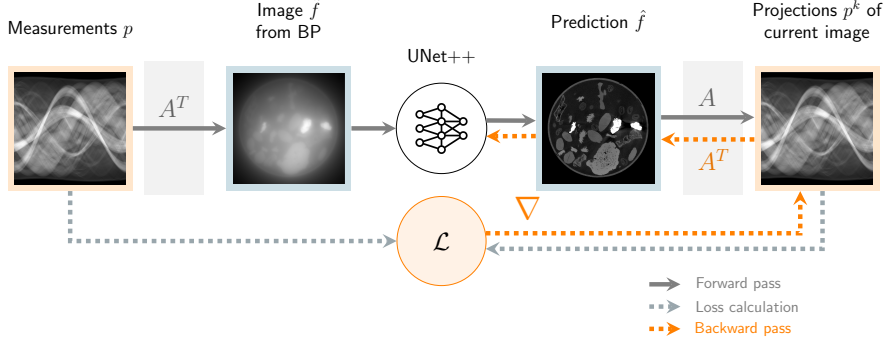


Fig. 2 Proposed unsupervised training scheme. The colored boxes indicate the domain of the respective data (orange projection domain, blue image domain). The boxes gray indicate the domain transform by FP (A) or BP (A^T). The steps to iteratively adapt the UNet++ weights are indicated by arrows.

the FP layer A that is applied on the image \hat{f} . Thus, the reconstructed data \hat{f} is represented in the projection data \hat{p} . Hence, \mathcal{L}_2 -loss calculations can be performed in the projection domain without the need for an image-domain ground truth. The backward pass propagates the calculated scalar loss value through the predicted projection tensor \hat{p} , the BP layer A^T and the predicted image tensor \hat{f} into the network layers. For training, the ADAM optimizer was used with a learning rate of 10^{-4} on an NVIDIA RTX A6000 GPU with 48 GB of VRAM, and no augmentations were applied to maintain physical and geometrical consistencies. We utilized a batch size of 8 training samples due to VRAM limitations. During training, the currently best performing network w.r.t. the validation data was stored and training was performed until the validation metrics did not decline for 100 epochs. All networks presented in the results of this work were trained between 330 and 480 epochs.

Comparing Figure 1 and Figure 2, the current training prediction \hat{f} coincides with the gradient-based IR current image f^k . The IR loss and the training loss are computed with the same formula from Eq. 3. This similarity was previously exploited for reconstruction of separated datasets in learned IR methods. Instead of altering the image itself, in network training, the gradient only affects the network’s weights. In contrast to unrolled optimization and DIP methods, when training is performed with many datasets, the network should be able to generalize the filter step. Hence, the main difference to learned IR methods is also the main advantage of our approach: Once trained, the network knows how to calculate the high-quality image from the blurry initial image f in a single step. Compared to IR or learned IR, this eliminates the need for computationally extensive gradient calculations or auto-differentiation steps after training completely.

Data and reconstruction

For validation of the proposed unsupervised training approach, the publicly available 2DeteCT[17] dataset is employed. It is tailored for advancing machine learning techniques in CT image reconstruction, artifact reduction, and segmentation. The dataset

includes over 5,000 CT reconstructed 2D FBP slices and their respective 2D projection data. The projections of each slice were acquired with three varying radiation parameter modes. We considered two of the three given modes in this work: High precision mode (90 kVp, Thoraeus filter of Sn=0.1 mm, Cu=0.2 mm, Al=0.5 mm) and beam-hardening affected mode (60 kVp, no filtration).

We employ 2800 of the 5000 provided slices and respective projection data, since a slight difference in geometry has been reported for the other measurements. This poses a critical difference for the reconstruction network since the FP and BP layers, as of now, are designed as fixed. To keep validation times during training short, we choose 100 projection datasets for validation between epochs for training supervision and early stopping. 2400 projection datasets are used for training. Approximately 10% of the available data (300 test datasets) are used for evaluation.

To compare our approach to conventional methods, we employ FBP with a Hann filter (with cut-off at 80% of normalized maximal frequency) and gradient-based maximum likelihood (ML) reconstruction. The FBP is calculated with our in-house software based on the *Reconstruction Toolkit*[18] whose projectors are parallelized on GPU. The ML optimization is performed with *SciPy*'s[19] L-BFGS-B implementation without bound conditions or regularization. The loss and gradient computations from Eq. 3 and Eq. 4 are calculated with the adapted *Parallelproj* projectors as well as the explicit gradient formula. We choose 100 iterations for ML optimization, which poses a good trade-off between image quality and reconstruction time in initial results: The norm of the gradients at the end of optimization calculates to an average of approx. $1.2 \cdot 10^{-7}$ ($\pm 4.2 \cdot 10^{-8}$) and an average pixel value change of approx. 0.6% for subsequent reconstructed images, which implies sufficient convergence. Additionally, we perform a supervised deep learning approach, which employs the same network architecture, but is trained with the \mathcal{L}_2 loss w.r.t. the (ground-truth) FBP images instead of projection data. This poses a significant advantage of prior information and can even be interpreted as the best-case deep learning approach for Experiment A, since the exact ground-truth information is used for calculation of the training loss.

Results

Experiment A: Reconstruction of FP data

Experiment A was evaluated in multiple stages. Since this experiment was conducted with forward projected data for which the exact geometry was known for both forward and backward projection, we can assume perfect alignment of projected and reconstructed data with our ground truth.

As the first stage, the general behavior of our method concerning projection domain loss minimization is investigated. Figure 3 shows a qualitative example of the projection data network prediction versus the ground-truth data. The exemplary difference image as well as the quantitative MSE evaluation in Figure 4 show that our method indeed predicts projection data that is highly similar to the ground-truth projection data. In Figure 3(c), slight overestimation can be observed in the center of the sinogram and underestimation in its edge regions. We compare our method's results to performing FBP and gradient-descent ML as well as a supervised DL approach on the

forward projected data. Our method performs significantly better than ML and FBP as calculated with a one-sided Wilcoxon rank test, which results in $p \ll 0.05$ in both cases (FBP: $p = 3.2 \cdot 10^{-3}$, ML: $p = 3.8 \cdot 10^{-7}$).

Second, the quantitative deviation of the reconstructed images to the ground-truth images was evaluated. The results for MSE and SSIM are presented in Figure 5. The distributions of MSE and SSIM values across methods appear similarly shaped. It could be observed that the images reconstructed by our unsupervised network show lower MSE and higher SSIM values than those obtained with alternative methods. The supervised method outperforms our approach, while producing noticeable high-deviation outliers. The relative trend of the distributions in Figure 4 and Figure 5 is consistent across domains and metrics.

Third, the reconstructed images were evaluated qualitatively. In Figure 6, a dataset of high deviation to the ground-truth image was evaluated. The figure shows the comparison across methods and the corresponding difference images for a whole reconstructed slice as well as an enlarged region for further inspection. High image quality can be observed in all reconstructions. The difference images reveal that while FBP and ML exhibit a typical noise level all over the reconstructed image, the predicted images for the supervised and our unsupervised approach mostly show differences in higher density regions.

To further investigate the noise properties in these images, Figure 7 shows the distribution of two exemplary regions that are assumed to be of a constant image value. Here, more deviation from the ground-truth mean value (marked as a vertical line) indicates a higher standard deviation and hence a higher noise level. As highlighted by the shadowed regions, similar to the supervised network, our approach reduced the standard deviation while adhering closely to the correct mean value. While not reproducing the ground-truth image exactly, this behavior suggests that the network produces smoother imaging results than FBP and ML.

Experiment B: Reconstruction of real data

In Experiment B, real beam-hardening affected projection data was used for reconstruction. Again, the projection domain difference to the ground-truth data was evaluated. Figure 8 shows the distribution of MSE of the test datasets for all three considered methods. It can be observed that, in terms of similarity to raw data, FBP and ML perform slightly worse than the network reconstruction. It should be noted

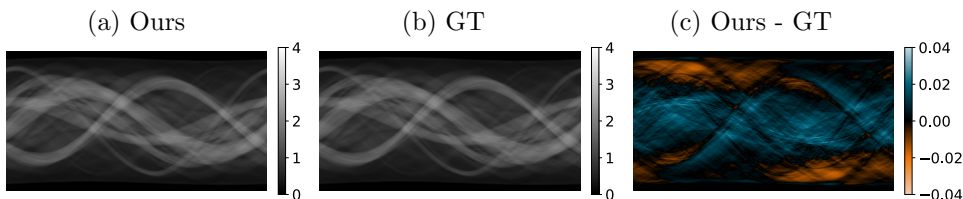


Fig. 3 Exemplary visualization of (a) predicted projection data, (b) ground-truth projection data, and (c) difference. Image values are unit-less since they indicate relative attenuation behavior to the unattenuated beam intensity.

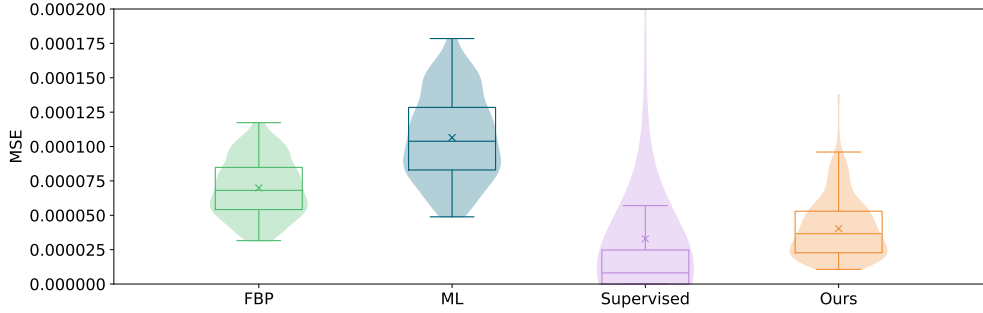


Fig. 4 MSE distribution of 300 projection predictions from test dataset w.r.t. ground-truth projection data. Values in the projection domain are unit-less.

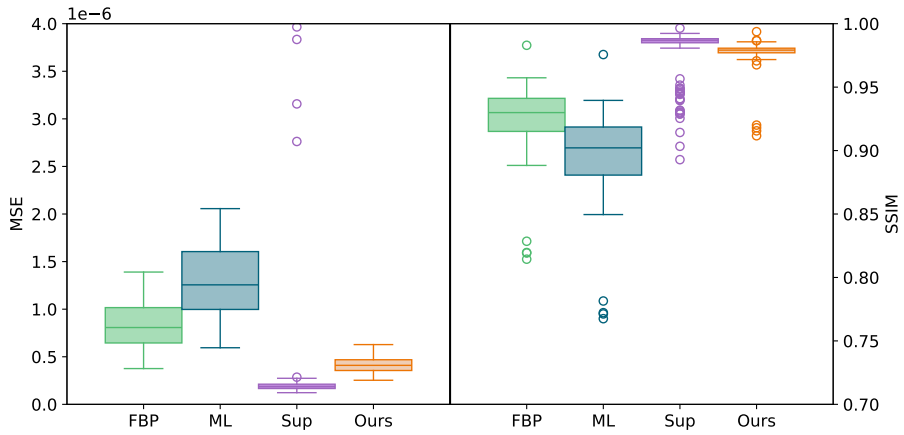


Fig. 5 Quantitative results in image domain for radon inversion task on 300 test images. All methods are calculated based on forward projected data of ground-truth image. Deviations are calculated with respect to said ground-truth image. $[MSE] = 1/cm^2$

here that the reconstruction for our method is pure network inference. For a number of 10 reconstructions, we observe a mean reconstruction time of 438 ms (± 51 ms) per dataset for the network reconstruction, whereas FBP takes 1717 ms (± 47 ms) and ML reconstruction takes approx. 63 400 ms ($\pm 2 200$ ms) on average.

The given image slices from the 2DeteCT dataset using FBP merely pose one possible reconstruction result. Thus, there exists no true ground-truth image information in Experiment B and the quantitative MSE evaluation in the image domain should be omitted. Instead, we can qualitatively compare performance by evaluating FBP reconstructions from high-quality raw data mode (as was used in Experiment A). We indicate this "ground-truth" image with the abbreviation GT*. Figure 9 shows the

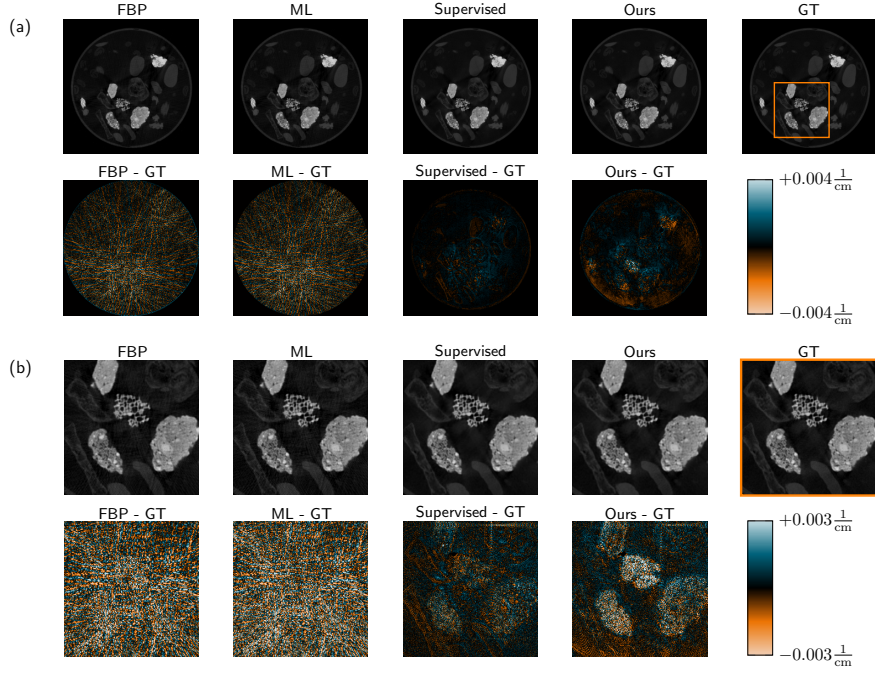


Fig. 6 Reconstructed images for different methods. The image was chosen as one of the worst MSE values ($MSE = 6.8 \cdot 10^{-7} \frac{1}{\text{cm}^2}$) between our method's result and the ground-truth (GT) image. First row in (a) is shown in level/window= $0.03/0.06 \frac{1}{\text{cm}}$. The orange rectangle indicates the ROI for Figure (b). First row in (b) shown in level/window= $0.05/0.1 \frac{1}{\text{cm}}$.

qualitative comparison in the image domain. Since the images look very similar, difference images to our method highlight their differences. The deviations seem to lie mostly in edges, higher density as well as artifact regions. The orange arrows in Figure

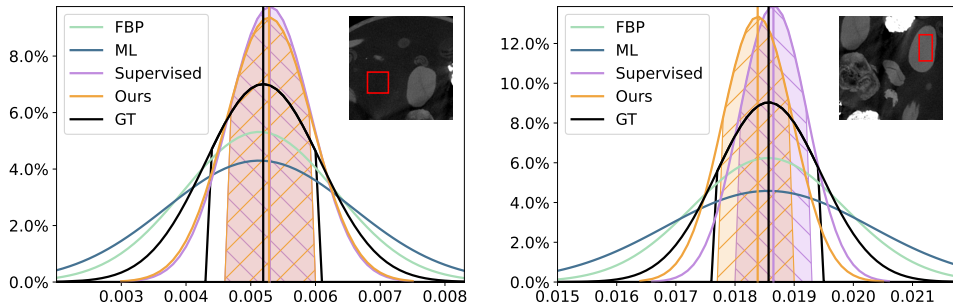


Fig. 7 Image value distribution of two exemplary constant image regions for different methods. The region of interest (ROI) is marked in red. Gaussian distribution curves are fitted to emphasize distribution differences. The black vertical lines indicate the mean value and standard deviation of the ground-truth image in the ROI. The colored vertical lines indicate the supervised's mean value. The shadowed regions indicate the standard deviation of the supervised network (pink) and the proposed unsupervised method (orange).

9(b) indicate that some details might get lost in our approach due to smoothing - which was observable in the noise analysis of Experiment A as well. In summary, our method performs subjectively similarly in the image domain while quantitatively outperforming in the projection domain and needing a fraction of the reconstruction time of conventional ML.

Discussion

Does our approach perform better than FBP and ML in Experiment A?

Yes. The ground-truth image in this case is the mathematically optimal solution for the pure Radon inversion task. As can be observed in Figure 5 and Figure 6 the network predicts reconstructed images that are closer to the ground-truth than FBP and ML. The supervised networks performs similarly with slightly better results. It is noticeable that uncertainty arises mainly in higher density material regions.

For high-quality data, as provided in Experiment A, FBP outperforms ML. We assume that this is due to the high quality of the underlying data, such that FBP performs well. Additionally, the stopping criterion for ML convergence has been configured such that optimization time does not become unreasonably long. It is expected that a higher number of iterations will outperform FBP in this case. As can be observed in the real-data case (Experiment B), ML does provide better results with the same tolerance choices and number of iterations for real beam-hardening affected data. The noise analysis in Figure 7 shows that the deep learning methods tend to smooth images more than FBP and ML. In total, in this constructed scenario with perfect knowledge of geometry and expected image values, the unsupervised network outperforms traditional methods.

How does the approach perform in Experiment B? Figure 8 shows that adherence to the raw projection data is better for our reconstruction network than FBP, ML and the supervised approach (Wilcoxon rank test, FBP: $p = 3.0 \cdot 10^{-8}$, ML: $p = 1.9 \cdot 10^{-4}$, Sup: $p = 9.3 \cdot 10^{-10}$). The inferior performance of the supervised

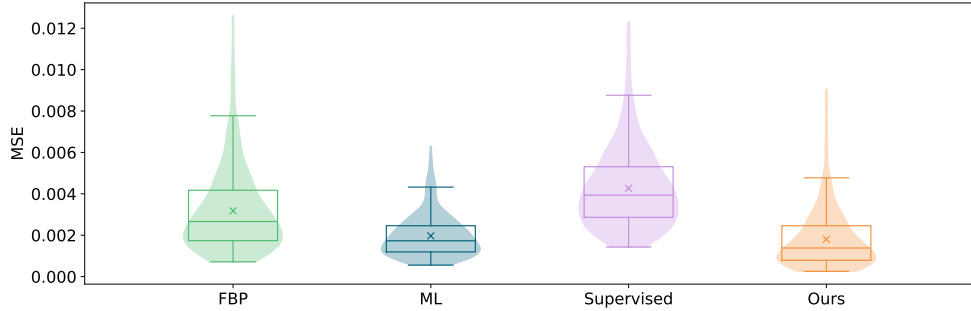


Fig. 8 Evaluation of Experiment B in projection domain. MSE distribution (w.r.t. ground-truth raw data) of 300 forward projected images from test dataset for different reconstruction methods. Values in the projection domain are unit-less.

approach is not surprising, as the network can at best match the reconstruction quality of the given FBP images. A detailed investigation of the MSE distribution showed that especially background noise was reduced by the deep learning approaches. When inspecting images in Figure 9, some details seem lost in reconstruction for both the supervised and the proposed unsupervised method. We hypothesize this behavior stems from the observed tendency of smooth reconstructed images, as shown in Figure 7 for Experiment A. It is to be investigated if insufficient fine-tuning of the networks or other factors are the reason for these differences in detail resolution. Overall, our approach performs similarly to the established methods while reducing reconstruction time significantly. Compared to supervised training, image quality is only slightly inferior.

We highlight that these results are very promising considering the different prerequisites between the supervised method, which relies on seldom-available ground-truth image information, and the proposed unsupervised method, which requires only the measured data and the reconstruction geometry. It should be mentioned that the networks performance can still be improved and fine-tuned by additional samples e.g. in an online training approach. Of course, the reconstructed images from our approach could also be used as initial images for conventional iterative reconstruction to reduce the number of iteration steps.

Limitations

The proposed approach presents several notable limitations. Firstly, this work is confined to two-dimensional reconstructions. For three-dimensional scenarios, substantial GPU memory will be necessary, which results in increased hardware requirements for effective implementation. The approach operates within a fixed geometric framework, which limits the amount of applicable data immensely. Additionally, in this work, no data augmentations were applied. These usually increase the network’s ability to generalize across different datasets. While the training process is time-consuming, the application of the trained network for reconstruction is executed with notable speed. These limitations indicate areas for potential improvement and further research to enhance the overall efficacy of the method.

Future work

Based on the observed limitations, we propose the following advancements for our future work. To expand to 3D reconstruction, the approach should be tested with cone-beam CT datasets for which raw data is available. A detailed description of the projection geometry is needed for such a dataset as well. Additionally, high variability of the data and the availability of augmentations will help achieve a stable and high-performing network. Another interesting advancement would be the inclusion of an additional network in the projection domain. The geometry of the projection layers should be adaptable to the dataset, which will increase the amount of suitable data. This can easily be realized but needs either additional computations when switching

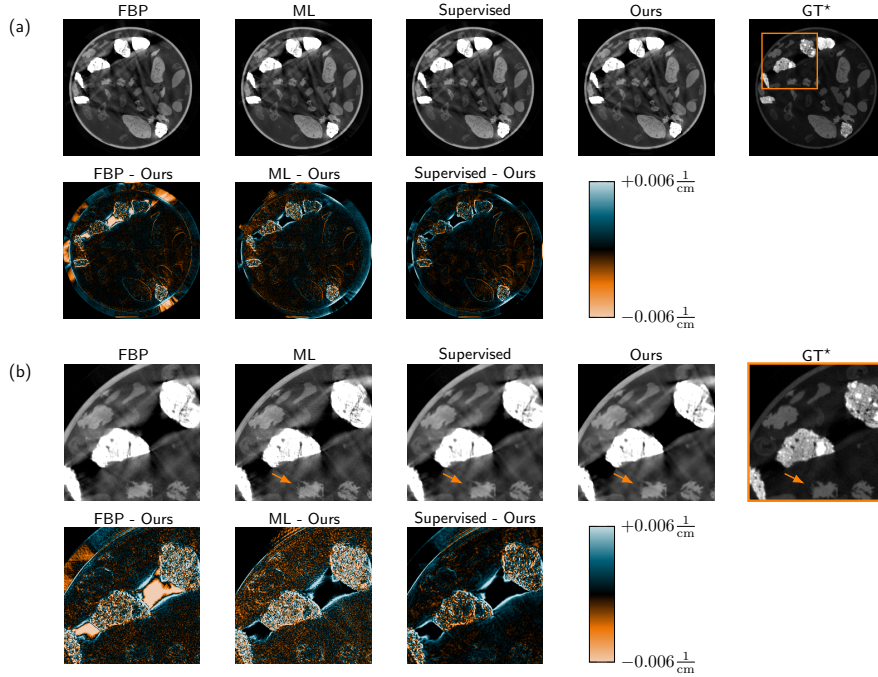


Fig. 9 Reconstructed images for different methods in level/window= $0.03/0.06 \frac{1}{\text{cm}}$. The ground-truth (GT*) image is generated from high-quality acquisition mode projection data without beam-hardening. Difference images are shown w.r.t. our method. The orange rectangle in Figure (a) indicates the ROI shown close-up in Figure (b).

datasets or larger memory for different pre-calculated projection layers. These additional resources could be realized with multi-GPU parallelization, which was out of the scope of this work.

Overall, the inclusion of unsupervised neural networks into image reconstruction creates new opportunities for image manipulation and use-case adaptation. This holds especially in comparison to conventional iterative methods, where regularizing terms and image gradients have to be designed carefully and computed expensively. While, in this work, we focused on the specific problem of CT imaging, the general approach of unsupervised training can be transferred to arbitrary inverse problems for which a continuous formulation of the forward problem (i.e. Eq. 2) can be modeled.

Data statement

All data analyzed in this study are included in the referenced article from *Kiss et al.*[17]. To provide detailed algorithm and parameter choices, we uploaded a minimal working example of our method to <https://gitlab.cc-asp.fraunhofer.de/imte-public/tomographicmethods/unsuperviseddlreco>.

Author Contribution Statement

L.H. wrote the main manuscript text. L.H. and J.C.E. prepared figures and conceptualized the experiment setup. M.Sch. supported experiment design and evaluation. M.St. offered critical reviews and provided essential guidance in defining the research question. All authors critically reviewed the manuscript. Final proofreading was performed by T.M.B..

Author Statement

The authors declare no competing interests.

Funding

This work was partially funded by the state of Schleswig-Holstein through the project "Individualisierte Medizintechnik für bildgestützte, robotische Interventionen (IMTE 2)", project number: 125 24 009.

References

- [1] Kyong Hwan Jin et al. "Deep Convolutional Neural Network for Inverse Problems in Imaging". In: *IEEE Transactions on Image Processing* 26.9 (2017), pp. 4509–4522. DOI: [10.1109/TIP.2017.2713099](https://doi.org/10.1109/TIP.2017.2713099).
- [2] Ji He and Jianhua Ma. *Radon Inversion via Deep Learning*. 2018. DOI: [10.48550/ARXIV.1808.03015](https://doi.org/10.48550/ARXIV.1808.03015). URL: <http://arxiv.org/abs/1808.03015>.
- [3] Yinsheng Li et al. "Learning to Reconstruct Computed Tomography Images Directly From Sinogram Data Under A Variety of Data Acquisition Conditions". In: *IEEE Transactions on Medical Imaging* 38.10 (Oct. 2019), pp. 2469–2481. ISSN: 1558-254X. DOI: [10.1109/tmi.2019.2910760](https://doi.org/10.1109/tmi.2019.2910760). URL: <http://dx.doi.org/10.1109/TMI.2019.2910760>.
- [4] Yongshuai Ge et al. "ADAPTIVE-NET: deep computed tomography reconstruction network with analytical domain transformation knowledge". In: *Quantitative Imaging in Medicine and Surgery* 10.2 (Feb. 2020), pp. 415–427. ISSN: 2223-4306. DOI: [10.21037/qims.2019.12.12](https://doi.org/10.21037/qims.2019.12.12). URL: <http://dx.doi.org/10.21037/qims.2019.12.12>.
- [5] Dmitry Ulyanov, Andrea Vedaldi, and Victor S. Lempitsky. "Deep Image Prior". In: *CoRR* abs/1711.10925 (2017). arXiv: [1711.10925](https://arxiv.org/abs/1711.10925). URL: <http://arxiv.org/abs/1711.10925>.
- [6] Yi Zhang et al. *LEARN++: Recurrent Dual-Domain Reconstruction Network for Compressed Sensing CT*. 2020. DOI: [10.48550/ARXIV.2012.06983](https://doi.org/10.48550/ARXIV.2012.06983). URL: <https://arxiv.org/abs/2012.06983>.
- [7] Yafen Li et al. "Comparison of Supervised and Unsupervised Deep Learning Methods for Medical Image Synthesis between Computed Tomography and Magnetic Resonance Images". In: *BioMed Research International* 2020.1 (Jan. 2020). Ed. by Zhiguo Zhou. ISSN: 2314-6141. DOI: [10.1155/2020/5193707](https://doi.org/10.1155/2020/5193707). eprint: [2314-6141](https://doi.org/10.1155/2020/5193707). URL: <http://dx.doi.org/10.1155/2020/5193707>.

- [8] Jonas Adler and Ozan Öktem. “Learned Primal-Dual Reconstruction”. In: *IEEE Transactions on Medical Imaging* 37.6 (2018), pp. 1322–1332. DOI: [10.1109/TMI.2018.2799231](https://doi.org/10.1109/TMI.2018.2799231).
- [9] Gregory Ongie et al. “Deep Learning Techniques for Inverse Problems in Imaging”. In: *IEEE Journal on Selected Areas in Information Theory* 1.1 (2020), pp. 39–56. DOI: [10.1109/JSAIT.2020.2991563](https://doi.org/10.1109/JSAIT.2020.2991563).
- [10] Richard Schoonhoven et al. “How auto-differentiation can improve CT workflows: classical algorithms in a modern framework”. In: *Opt. Express* 32.6 (Mar. 2024), pp. 9019–9041. DOI: [10.1364/OE.502920](https://doi.org/10.1364/OE.502920). URL: <https://opg.optica.org/oe/abstract.cfm?URI=oe-32-6-9019>.
- [11] M. Bertero et al. *Introduction to Inverse Problems in Imaging (2nd Edition)*. CRC Press, 2021. Chap. Iterative Methods, pp. 105–130. DOI: [10.1201/9780367806941](https://doi.org/10.1201/9780367806941).
- [12] Adam Paszke et al. *PyTorch: An Imperative Style, High-Performance Deep Learning Library*. 2019. arXiv: [1912.01703](https://arxiv.org/abs/1912.01703) [cs.LG]. URL: <https://arxiv.org/abs/1912.01703>.
- [13] Georg Schramm and Kris Thielemans. “PARALLELPROJ - an open-source framework for fast calculation of projections in tomography”. en. In: *Front. Nucl. Med.* 3 (2023), p. 1324562. DOI: [10.3389/fnume.2023.1324562](https://doi.org/10.3389/fnume.2023.1324562). URL: <https://github.com/gschramm/parallelproj>.
- [14] Zongwei Zhou et al. *UNet++: A Nested U-Net Architecture for Medical Image Segmentation*. 2018. arXiv: [1807.10165](https://arxiv.org/abs/1807.10165) [cs.CV]. URL: <https://arxiv.org/abs/1807.10165>.
- [15] Saining Xie et al. “Aggregated Residual Transformations for Deep Neural Networks”. In: *CoRR* abs/1611.05431 (2016). arXiv: [1611.05431](https://arxiv.org/abs/1611.05431). URL: <http://arxiv.org/abs/1611.05431>.
- [16] Pavel Iakubovskii. *Segmentation Models PyTorch*. https://github.com/qubvel/segmentation_models.pytorch. 2019.
- [17] Maximilian B. Kiss et al. “2DeteCT - A large 2D expandable, trainable, experimental Computed Tomography dataset for machine learning”. In: *Scientific Data* 10.1 (Sept. 2023), p. 576. ISSN: 2052-4463. DOI: [10.1038/s41597-023-02484-6](https://doi.org/10.1038/s41597-023-02484-6). URL: <https://doi.org/10.1038/s41597-023-02484-6>.
- [18] S Rit et al. “The Reconstruction Toolkit (RTK), an open-source cone-beam CT reconstruction toolkit based on the Insight Toolkit (ITK)”. In: *Journal of Physics: Conference Series* 489 (Mar. 2014), p. 012079. ISSN: 1742-6596. DOI: [10.1088/1742-6596/489/1/012079](https://doi.org/10.1088/1742-6596/489/1/012079). URL: <http://dx.doi.org/10.1088/1742-6596/489/1/012079>.
- [19] Pauli Virtanen et al. “SciPy 1.0: Fundamental Algorithms for Scientific Computing in Python”. In: *Nature Methods* 17 (2020), pp. 261–272. DOI: [10.1038/s41592-019-0686-2](https://doi.org/10.1038/s41592-019-0686-2).